

Correlation between Surface Reactions and Electrochemical Performance of Al₂O₃- and CeO₂-Coated NCM Thin Film Cathodes

Hendrik Hemmelmann, Raffael Ruess, Philip Klement, Jörg Schörmann, Sangam Chatterjee, Joachim Sann, and Matthias T. Elm*

Depositing ultrathin oxide coatings has been proven a successful approach to stabilize the surface of LiNi_xCo_yMn_zO₂ active cathode material in lithium-ion batteries (LIB). The beneficial effect of Al₂O₃ coatings arises at least partly from spontaneous reactions between coating and liquid electrolyte. However, it remains unclear if comparable surface reactions occur for other oxide coatings. One difficulty is the characterization of reaction products at the cathode–electrolyte interface due to the multi-phase properties of composite cathodes. Here, thin films are utilized as model systems to correlate surface reactions with the performance of Al₂O₃- and CeO₂-coated nickel cobalt manganese oxides (NCM). Electrochemical characterization confirms that an Al₂O₃ coating improves long-term cycling stability, while CeO₂-coated thin films perform even worse than uncoated counterparts. The analysis of the surface reaction products using X-ray photoelectron spectroscopy shows that both coatings are fluorinated upon contact with liquid electrolyte in agreement with thermodynamic considerations. The fluorinated Al₂O₃ coating is stable during cycling, resulting in the improved cell performance. In contrast, the fluorinated CeO₂ coating changes chemical composition, facilitating corrosion of the NCM surface. The results demonstrate the importance of a detailed analysis of surface reactions to evaluate the suitability of ultrathin oxide layers as protective coatings for LIBs.

mobile devices. They achieved a high capacity of around 160 mAh g⁻¹ and a high rate capability by utilizing lithiated graphite as anode material, a liquid electrolyte, and lithium cobalt oxide (LCO) as cathode material.^[1] Since then, the demand for mobile energy storage has tremendously skyrocketed, necessitating the development of next-generation LIBs with higher energy densities and enhanced cycle life.^[2–5] Thus, lithium nickel cobalt manganese oxides (NCM) emerged as a new class of cathode materials isostructural to LCO. With the substitution of Co for Ni and Mn in different fractions, the electrochemical properties of NCM materials are tunable with respect to their designated purpose.^[6,7] In particular, LiNi_{0.33}Co_{0.33}Mn_{0.33}O₂ (NCM111) is the focus of research since it shows improved rate capability and increased capacity compared to LCO.

While this sounds promising, there are downsides of NCM materials. Repeating intercalation and deintercalation of Li⁺ ions lead to changes in the crystal structure, rendering sections of the material

electrochemically inactive.^[8] A variety of corrosion reactions and degradation phenomena at the electrode–electrolyte interface accompany these structural changes. Organic parts of the liquid electrolyte decompose, forming a solid–electrolyte

1. Introduction

With the introduction of the lithium ion battery (LIB) in 1991, SONY presented an efficient and rechargeable battery for

H. Hemmelmann, R. Ruess, P. Klement, J. Schörmann, S. Chatterjee, J. Sann, M. T. Elm
 Center for Materials Research
 Justus-Liebig-University Gießen
 Heinrich-Buff-Ring 16, 35392 Gießen, Germany
 E-mail: matthias.elm@phys.chemie.uni-giessen.de

 The ORCID identification number(s) for the author(s) of this article can be found under <https://doi.org/10.1002/admi.202202268>.

© 2023 The Authors. Advanced Materials Interfaces published by Wiley-VCH GmbH. This is an open access article under the terms of the Creative Commons Attribution License, which permits use, distribution and reproduction in any medium, provided the original work is properly cited.

R. Ruess, J. Sann, M. T. Elm
 Institute of Physical Chemistry
 Justus-Liebig-University Gießen
 Heinrich-Buff-Ring 17, 35392 Gießen, Germany
 P. Klement, J. Schörmann, S. Chatterjee, M. T. Elm
 Institute of Experimental Physics I
 Justus-Liebig-University Gießen
 Heinrich-Buff-Ring 16, 35392 Gießen, Germany

DOI: 10.1002/admi.202202268

interface (SEI).^[9–11] While the formation of a SEI on the anode side is actually desired and can be tailored to a certain extent where it benefits the performance of the cell,^[12,13] side reactions on the cathode side reduce the access of Li⁺ ions to the host material due to the formation of an insulating cathode–electrolyte interface (CEI). Moreover, the CEI incorporates corrosion products, which arise from acidic attack of the cathode by hydrofluoric acid (HF).^[14,15] HF is formed when using LiPF₆ as conductive salt in the electrolyte LP30. Even small amounts of water in the cell generate HF, which corrodes the cathode surface, leading to the formation of metal fluorides and HF again.^[16,17] Consequently, these side reactions lead to capacity fading and therefore diminish the energy storage capability of the cathode material.

Different approaches have been developed to address this issue. For example, changing the conductive salt of the electrolyte to LiB[C₂O₄]₂ (LiBOB) or LiClO₄ prevents HF formation by removing fluorine from the solution,^[18,19] while the incorporation of dopants (like Zr⁴⁺, Mg²⁺ or Ti⁴⁺) into the NCM structure shows promising results toward stabilizing the cathode active material.^[20–23] One of the most prominent approaches, however, is the deposition of an artificial CEI to protect the surface of the cathode material. An ultrathin protective coating hinders the corrosive species from directly attacking the surface of the cathode active material (CAM) and, thus, prevents the dissolution of the transition metals.^[24–26] However, it also results in an initial increase of the overall cell resistance, as Li⁺ ions have to pass through the coating during cycling. Potential coating materials range from lithium containing coatings like LiNbO₃ featuring a moderate Li⁺ ion conductivity to insulating and chemically inert materials like Al₂O₃, CeO₂, or ZrO₂.^[27–33] The coatings enhance the cycling stability of the cathode and, thus, the overall electrochemical performance improves in all cases, regardless of the chemical nature of the coating.

Finding promising coating materials is often phenomenological in nature. 2D thin films are needed as model systems in order to analyze the surface properties with methods of high surface sensitivity, like X-ray photoelectron spectroscopy (XPS) or secondary ion mass spectrometry (SIMS) as an in-depth analysis of ultra-thin surface coatings of less than 2 nm thickness is difficult for spherical cathode particles.^[34,35] The detailed spectroscopic study of the surface properties enables the investigation of reactions occurring at the electrolyte–cathode or electrolyte–coating interfaces. More and more research groups take this approach to get a fundamental understanding of interface processes in battery systems without the need to consider complicating factors such as the influence of binder materials or conductive additives.^[34,36–38] Another advantage of 2D thin films is the inherent quasi-one-directional transport path of the charge carriers (Figure 1) which facilitates the interpretation of, for example, electrochemical impedance measurements.

In particle-based composite cathodes, the electrons have to pass through the CEI and the residuals formed on the conductive additives when moving between the NCM particle and the current collector as schematically depicted in Figure 1a. In contrast, the electrons in thin film model cathodes move only inside the cathode active material before reaching the current collector (Figure 1b). There is no interference with the CEI formed at

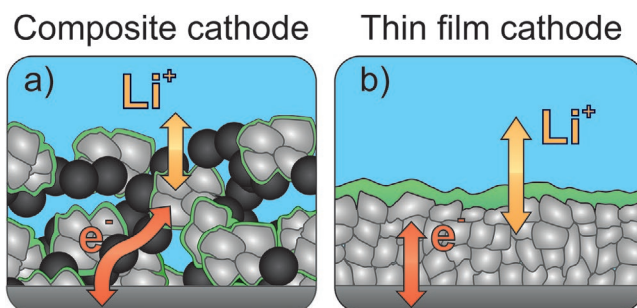
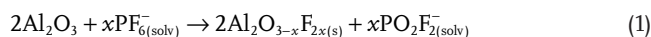


Figure 1. Schematic illustration of the transport pathways of electrons and Li⁺ ions a) in a composite cathode containing carbon conductive additive (black) and b) in a thin film cathode. The CEI is depicted in green.

the surface. Thus, thin films are ideally suited to identify the impact of CEI formation on the charge transfer resistance at the NCM surface as only the ion transport is affected.

Here, we investigate the influence of Al₂O₃ and CeO₂ coatings on the electrochemical performance of NCM cathode materials. NCM111 thin films prepared via a sol-gel process using spin coating act as suitable model system.^[30] The coatings were deposited using atomic layer deposition (ALD). As coating material, we chose Al₂O₃ as the most common oxide coating^[39–42] as well as CeO₂, which is currently also considered as a promising coating material.^[28,43] Electrochemical impedance spectroscopy (EIS) under defined conditions unravels the influence of Al₂O₃ and CeO₂ coatings on the transport processes in the CEI, which we correlate with the electrochemical performance of the NCM thin films. XPS characterization of both, the pristine and the coated thin film cathodes after prolonged contact with the electrolyte LP30 as well as after electrochemical treatment reveals spontaneous reactions between the cathode surface and the electrolyte. In agreement with the results by Hall et al. we observe that Al₂O₃ in contact with the electrolyte leads to the formation of a mixed aluminum oxyfluoride at the surface layer and lithium difluorophosphate:^[44]



In addition, Hall et al. proposed with the help of thermodynamic considerations that fluorination of the coating and formation of lithium difluorophosphate might occur for other oxide coatings as well. We show that this assumption holds true for the CeO₂-coated thin films, where fluorination of the surface happens and lithium oxyfluorophosphates form during cycling. In addition, we reveal that the fluorination of the Al₂O₃ coating has a stabilizing effect on the surface during cycling. In contrast, electrochemical cycling causes changes of the surface composition in case of CeO₂-coated samples. Thus, the fluorinated CeO₂ coating fails in preventing surface degradation resulting in a more pronounced capacity fading. The results provide a better understanding on the impact of oxide coatings on the degradation reactions at the CEI and, thus, contribute to devising a design strategy for suitable coating materials for applications in battery systems with liquid or solid electrolytes.

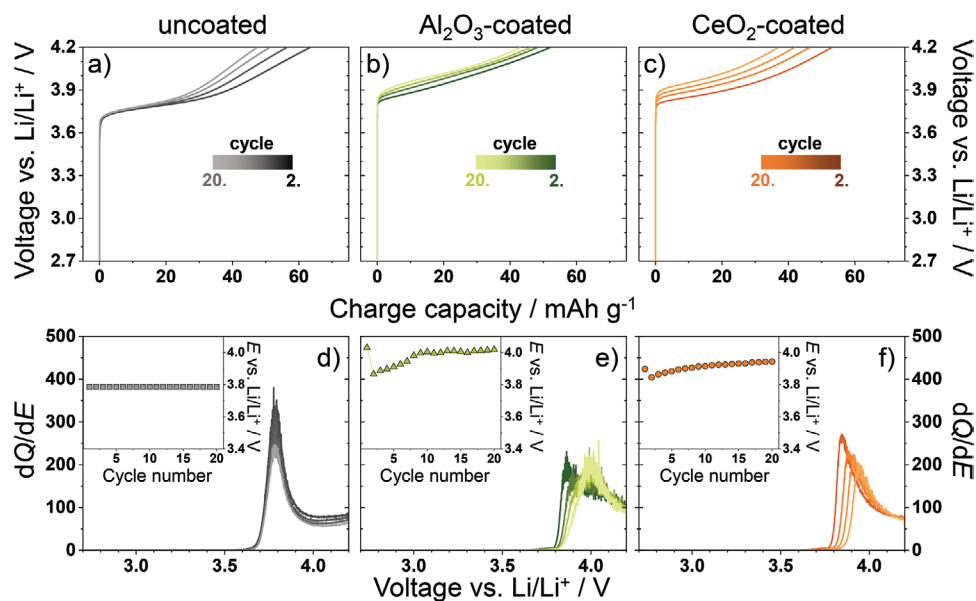


Figure 2. Charge profiles without the first cycle of a cell with a) an uncoated, b) an Al_2O_3 -coated, and c) a CeO_2 -coated thin film cathode. Corresponding differential capacity of the cells with d) an uncoated, e) an Al_2O_3 -coated, and f) a CeO_2 -coated thin film cathode. The insets exhibit the change in peak position with increasing cycling number.

2. Results and Discussion

2.1. Electrochemical Characterization of Oxide Coated Thin Film Cathodes

Figure 2a–c depicts the charging profiles of an uncoated NCM thin film and two thin film cathodes coated with 2 nm Al_2O_3 or CeO_2 , respectively. It is worth noting that the first cycle is not shown due to the well-known capacity drop occurring after the first cycle. To get a better insight in the charging behavior, the differential capacity dQ/dE of the three half cells are displayed in **Figure 2d–f**. The sample without protective coating (**Figure 2a**) exhibits the typical shape of a charge profile for NCM cathode materials.^[45] At around 3.7 V a plateau with a minor slope occurs which gets steeper when the potential reaches ≈ 3.8 V. The capacity of the uncoated sample fades over time although the overpotential is mostly constant. Interestingly, the peak in the differential capacity (**Figure 2d**) at ≈ 3.8 V shows virtually no voltage shift with increasing cycling number, indicating only a minor increase in the overpotential. For the Al_2O_3 -coated thin film (**Figure 2b**), the voltage experiences a steady but more or less constant increase, that is, no change in the slope is observed. Furthermore, an increase in polarization is evident for this sample, while the loss in capacity is diminished compared to the uncoated sample. Finally, the charging profile of the CeO_2 -coated thin film shown in **Figure 2c** exhibits a greater loss of capacity than the uncoated one from the second to the 20th cycle. The change in voltage during charging, however, resembles a more parabolic shape accompanied by a clear change in polarization. For the Al_2O_3 - (**Figure 2e**) and CeO_2 -coated (**Figure 2f**) cathodes a steady increase in the overpotential is found, which is also shown in the insets of **Figure 2**. The peak in the dQ/dE profile of the CeO_2 -coated sample shows an asymmetric shape, while the peak shape

in case of the Al_2O_3 -coated cathode cell stretches over a wide potential range. This indicates an inhomogeneous increase of the resistance, for example, due to changes in the contact area and/or the formation of a CEI, leading to a broader distribution of the cell resistance and therefore a broader peak. The capacity of the uncoated sample fades without an increase in the cell resistance, as evident by no peak shift in **Figure 2d**, whereas the cell resistance for the Al_2O_3 -coated sample (**Figure 2e**) increases without a major decrease in capacity. Moreover, the CeO_2 -coated sample exhibits a capacity fading while also showing a higher peak shift in **Figure 2f** associated with an increase in resistance. The analysis indicates a higher overpotential with ongoing cycling for the coated cells resulting in a higher resistance, which we investigated in more detail by electrochemical impedance spectroscopy as will be discussed later. However, the increase in overpotential and, thus, of the cell resistance is typically associated with a capacity fading over time.^[31,33,46–48] To check this assumption, **Figure 3** shows a comparison of the charge capacity with varying cycling numbers of the three different thin films.

The charge capacity in **Figure 3** is normalized to the charge capacity of the second cycle as the capacities of the cells vary slightly for each thin film due to difficulties in determining exactly the masses and thicknesses of the films.^[30] The non-normalized values are presented in **Figure S1**, Supporting Information of the SI. After 20 cycles, the Al_2O_3 -coated sample retains 82.6% of its charge capacity in the second cycle, while the uncoated and CeO_2 -coated samples retain 74.9% and 69.5%, respectively. Thus, the Al_2O_3 -coated thin film improves the stability of the cathode in a liquid electrolyte cell setup in agreement with literature.^[29,31,32,39,49,50] The CeO_2 -coated thin film experiences a huge capacity drop after the initial cycle and afterward performs with a higher capacity drop compared to the uncoated sample. This is in contrast to previous studies,

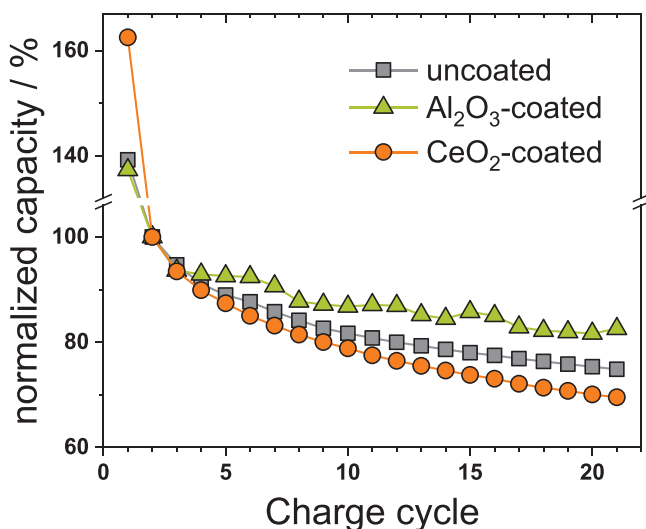


Figure 3. Decrease of the normalized charge capacity (normalized to the second cycle of each cell for better comparability) with increasing cycle number for cells with an uncoated (grey), an Al_2O_3 -coated (green), and a CeO_2 -coated (orange) thin film cathode.

which report on the improvement of the electrochemical performance of cathodes prepared from NCM secondary particles decorated with CeO_2 nanoparticles.^[28,29] As our thin films are coated with a homogenous CeO_2 layer, the observed discrepancy in the electrochemical performance indicates that besides

chemical composition, the morphological properties of the CeO_2 coating play a decisive role in improving the electrochemical performance as recently also reported for Al_2O_3 -based coatings.^[51,52] For example, Dannehl et al. discussed that the degree of coverage and the morphology of the particle coating can significantly affect the electrochemical properties of the active material.^[51] In addition, CeO_2 thin films deposited by ALD typically exhibit a certain non-stoichiometry depending on their thickness.^[53–55] This increases their chemical reactivity, which results in a faster degradation of the coating material. However, the capacity retention for the Al_2O_3 -coated sample is improved despite the increase in polarization with increasing cycling number, which arises only in the oxide coated thin film as discussed above (inset of Figure 2d–f). Electrochemical impedance measurements were carried out for an uncoated, an Al_2O_3 -coated, and a CeO_2 -coated NCM thin film after each charge-discharge cycle in order to identify the origin of the polarization increase. The corresponding Nyquist plots are presented in Figure 4a–c. Two semicircles are observable in all cases, one in the high-frequency region and one in the low-frequency region. The low-frequency region additionally features a Warburg impedance with an angle of $\approx 45^\circ$ for the uncoated sample, whereas it shows a lower angle for the coated ones. The slope of the Warburg impedance further decreases with increasing cycling number for both the Al_2O_3 - and the CeO_2 -coated samples, while it barely changes in case of the uncoated thin film. The Warburg impedance arises from ion diffusion inside the electrode.^[56,57] A decrease in the Warburg impedance indicates

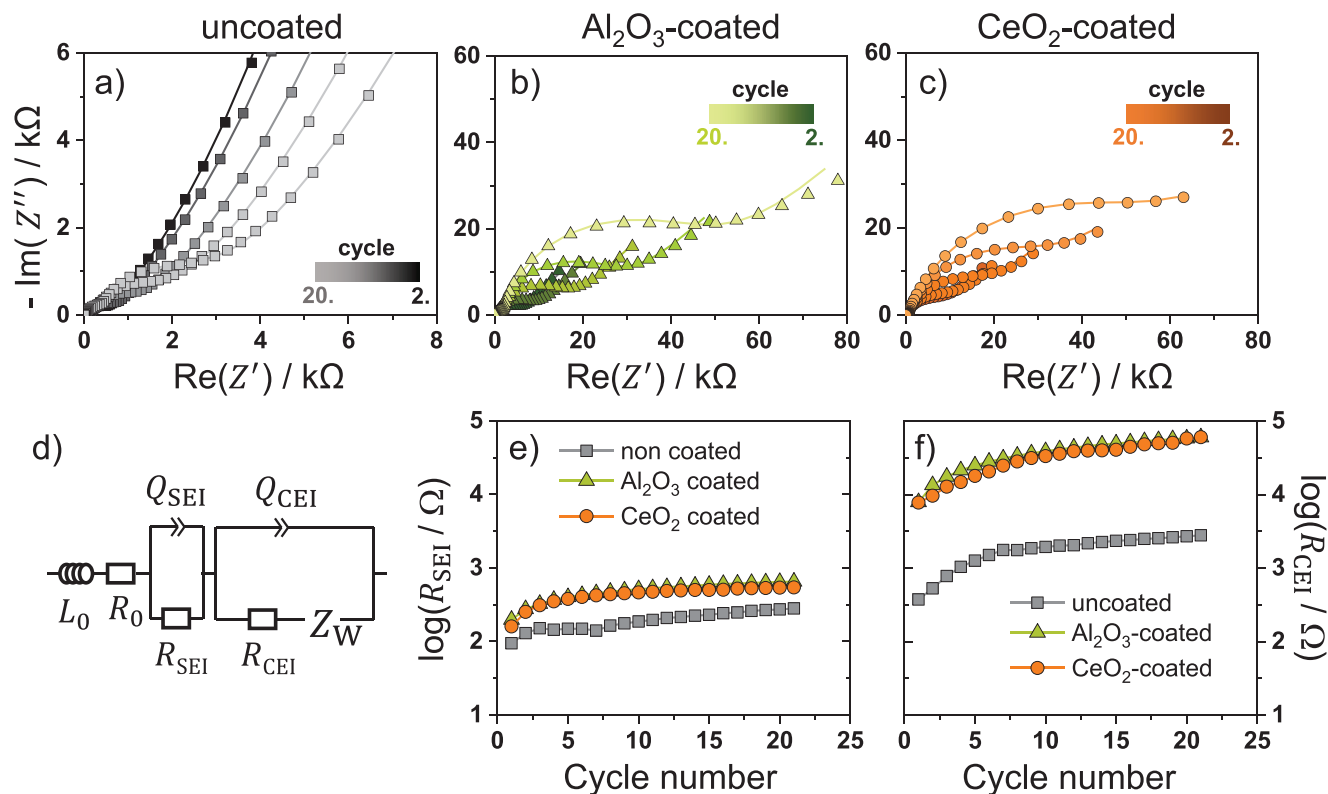


Figure 4. Nyquist plot with data points (dots) and fit (line) for a cell with a) an uncoated, b) an Al_2O_3 -coated and c) a CeO_2 -coated thin film cathode. The equivalent circuit to describe the data is depicted in (d). Evaluation of the resistance of e) the cathode side and f) the anode side in a logarithmic scale for better comparability.

changes in the diffusion process of the ionic species Li^+ .^[58,59] A tortuous diffusion path of the ions leading to a non-uniform lithiation of the cathode material is one reason for such changes in the Warburg impedance.^[60] It is known that NCM materials undergo a swelling and shrinking process during electrochemical cycling.^[57] Parts of the NCM surface can lose contact with the stable oxide coating layer due to the related volume change. This decreases the contact area and, thus, hinders Li^+ diffusion in the cathode material. In addition, changes in the Warburg tail also arise due to a non-homogenous growth of the CEI on coated NCM thin films, which also affects the diffusion pathways for Li^+ in the cathode material. The increase in cathode resistance with increasing cycling number, which is evident from the growing second semicircle in the Nyquist plot, further supports this assumption. For a more detailed analysis of the impedances, the impedance data are described using the equivalent circuit depicted in Figure 4d. L_0 represents the inductance of the cables and current collectors of the cell, while R_0 combines the ohmic resistances of anode, cathode, electrolyte, and current collectors. The first semicircle in the high-frequency range is attributed to the SEI formation at the anode and is described by a resistance R_{SEI} and a constant phase element Q_{SEI} connected in parallel. The second semicircle in the low-frequency range is attributed to the transport processes through the growing CEI at the cathode. It is represented by a Warburg element Z_W in series with a charge transfer resistance R_{CEI} , which are connected parallel to a constant phase element Q_{CEI} representing a non-ideal double layer capacity.^[61,62]

The change in the resistances R_{SEI} and R_{CEI} with increasing cycle number are depicted in Figure 4e,f, respectively, in a logarithmic scale. The other parameters extracted from the fitting procedure barely change during cycling and are presented in the SI (Figure S2, Supporting Information). As shown in Figure 4e, the increase of R_{SEI} during cycling is comparable for all three cells, with minor deviation of less than one order of magnitude, that is, the cell with the uncoated cathode material exhibits a lower resistance compared to the cells with coated cathodes. Different reaction products form (see Equation (1)) depending on the active material as well as the coating, which diffuses through the electrolyte to the anodes surface.^[63–65] This cross-talk effect influences the growth of the SEI at the anode side. Thus, it might be responsible for the different R_{SEI} of the pristine and coated cells. The change of R_{CEI} with increasing cycling number is shown in Figure 4f. For the cell with the uncoated cathode thin film, R_{CEI} increases by roughly one order of magnitude from 373 to 2781 Ω after 20 cycles. In the logarithmic representation, the increase in resistances is nearly linear. However, the slope changes after the seventh cycle. Nevertheless, the total increase in resistance by an applied current of 1.5 μA only results in an overpotential of about 4 mV. This explains the lack of a polarization increase (Figure 2a,d). For the cells with an Al_2O_3 -coated thin film cathode, R_{CEI} increases from about 7.9 to 60.0 k Ω during cycling, that is, the cells with coated NCM thin films exhibit a notably larger R_{CEI} compared to the uncoated one. A comparable change of R_{CEI} from 7.8 to 60.0 k Ω is also observed for the CeO_2 -coated thin film. However, R_{CEI} of all three cells show a comparable behavior with a change in slope after 7 cycles and an increase of approximately one order of magnitude during cycling.

The impedance measurements show that even a 2 nm thin alumina or ceria coating leads to a significant increase of R_{CEI} by a factor of about 20. The oxide coating not only protects the surface of the cathode active material from corrosion, but also impedes charge transfer of the Li^+ ions between electrode and electrolyte. However, only the transport of Li^+ is affected by the coating when using thin film cathodes (see Figure 1b), while the electrons also need to pass through the coating layer when using cathodes prepared from coated NCM secondary particles (Figure 1a). The same holds for the CEI formed during cycling due to side reactions between thin film and electrolyte, which only impacts the transport of the lithium ions. An increase of R_{CEI} with increasing cycle number may indicate a reduction of the electrochemically active contact area between active material and electrolyte, which often occurs due to changes in the cathode surface during cycling. Such a decrease in the contact area is also reflected in a change in the interface capacity, which can be calculated from the parameter α , the resistance R_{CEI} and the constant phase element Q_{CEI} .^[66–68]

$$C_{\text{CEI}} = R_{\text{CEI}}^{1-\alpha} Q_{\text{CEI}}^{1/\alpha} \quad (2)$$

As shown in Figure S3, Supporting Information, the capacity of the CEI (and of the SEI) shows only a minor change with increasing cycling number, that is, a large change of the active contact area can be excluded for our thin film cathodes. Thus, the increase of R_{CEI} can directly be related to changes in the thickness of the CEI. The uncoated cathode experiences a comparably low R_{CEI} for the ion transfer at the surface. This hints at a less stable or even unstable CEI. Thus, corrosion occurs accompanied by a loss in cathode active material, which is responsible for the capacity fading. The cycling performance of an Al_2O_3 -coated sample behaves more stable compared to the uncoated and CeO_2 -coated thin films, despite the much higher R_{CEI} of the coated thin films. It, thus, maintains a higher capacity. This indicates the formation of a more stable CEI at the aluminum oxide surface, which increases the ionic resistance for Li^+ ion transport while simultaneously protecting the cathode material from degradation. In case of the CeO_2 -coated thin film, the resistance also increases, while the capacity decreases over time. Therefore, the influence of the coating layer on the charge transfer is similar to the Al_2O_3 -coated thin films. However, the fading of the capacity indicates a less stable surface leading to a failure in its protective capabilities.

2.2. Analyzing Surface Reactions on Oxide Coatings

The detailed morphological analysis of the surface of the thin films after cycling confirms the interpretation of the impedance measurements (Figure 5). Before electrochemical cycling, all three types of cathodes show similar surface structures (Figure S4, Supporting Information). After 20 cycles, the uncoated thin film shows clearly visible cracks and in some areas, the NCM thin film is even lifted from the Pt current collector (Figure 5a). The structural damage arises as the NCM thin film experiences volume expansion and shrinkage during intercalation and deintercalation of Li ions. This effect is well investigated for NCM powders, where volume changes

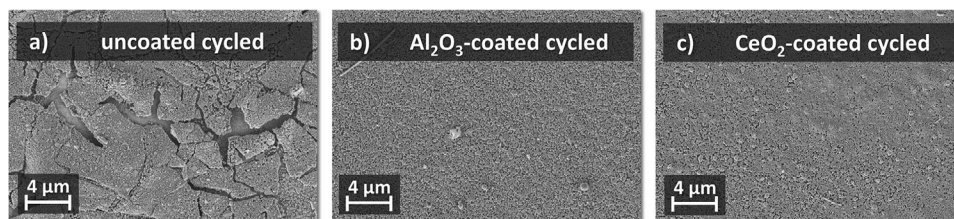


Figure 5. SEM micrographs of the cathode thin films a) without coating, b) with Al_2O_3 -coating, and c) with CeO_2 -coating after cycling for 20 cycles.

during cycling results in cracking of the NCM secondary particles.^[31,33,57,69,70] Due to the cracking, more active material gets exposed to the electrolyte and therefore is corroded by the acidic species in the electrolyte. Corrosion of the surface also influences the mechanical stability of the thin film and facilitates cracking.^[57,71] In contrast, coated thin films show no crack formation and no changes at all are observable after cycling for the Al_2O_3 -coated thin film (Figure 5b). The improvement of the structural stability of NCM by an Al_2O_3 coating is well investigated.^[31,33,50,72] The coating hinders direct contact between electrolyte and cathode. Consequently, less side reactions with the less stable and more reactive delithiated phase of NCM occur. Overall, the Al_2O_3 coating impedes the formation of electrochemical inactive material and, therefore, avoids mechanical stress due to the presence of different phases in the material. Also, the CeO_2 -coated thin film cathode (Figure 5c) shows no indications of cracking. However, we observe minor, bubble-like changes in the topography. As this occurs only in certain areas, it seems to be a randomized effect distributed over the whole surface. A possible explanation may be structural changes in the CeO_2 coating. While Al_2O_3 as a coating material is chemically stable, CeO_2 is known to exhibit a certain oxygen off-stoichiometry δ . In particular, ALD-derived $\text{CeO}_{2-\delta}$ thin films show a non-stoichiometry depending on their thickness.^[54,55] When Ce^{4+} is reduced to Ce^{3+} , for example by corrosion reactions with the HF in the electrolyte, its atomic radius changes from 0.97 Å to 1.14 Å.^[73,74] This results in chemical strain in the coating layer.^[75–77] In addition, some areas of the coating might not be able to withstand the expansion of the NCM material underneath leading to the bloated areas visible in the SEM picture (Figure 5c), damaging the dense coating and exposing the surface of the NCM to the electrolyte and its corrosive species.

To get further insights into the surface properties and to estimate the stability of the cathode coating, XPS investigations were performed. All three model cathodes, that is, the uncoated, the Al_2O_3 -coated, and the CeO_2 -coated NCM thin films, were analyzed in the pristine state, after being in contact with the electrolyte for 72 h, and after electrochemically charging and discharging for 20 cycles. In particular, thermodynamic considerations regarding the chemical stability of the Al_2O_3 and CeO_2 coating in contact with the electrolyte LP30 are helpful for the interpretation of the XPS measurements. Based on the results by Hall et al., Equation (1) is simplified due to a lack of thermodynamic data for aluminum oxyfluoride. For $x = 3$ the thermodynamic data are available as AlF_3 is formed:^[78]



Hall et al. calculated the Gibbs free energy change at standard conditions to be $\Delta G_{\text{Al}_2\text{O}_3}^\circ = -451 \text{ kJ mol}^{-1}$, that is, the reaction is exergonic and occurs spontaneously. Even small quantities of the as-formed LiPO_2F_2 improve the cell performance when using liquid electrolyte.^[79–81]

For CeO_2 getting into contact with LP30, the following simplified reaction can be assumed:



The Gibbs free energy for this reaction at standard conditions yields $\Delta G_{\text{CeO}_2}^\circ = -26 \text{ kJ mol}^{-1}$, that is, the formation of CeF_4 and PO_2F_2^- is exergonic and spontaneous. To elucidate if the thermodynamic considerations are reliable for estimating the stability of the cathode coatings, the Li 1s, the F 1s, as well as the Al 2p and the Ce 3d regions of the XPS measurements are analyzed in the following.

Figure 6 depicts the energy regions of the Li 1s (Figure 6a) and the F 1s (Figure 6b) core levels of a NCM thin film cathode without a protective coating in the pristine state (top row), after 72 h of exposure to LP30 (middle row), and after charging and discharging for 20 cycles (bottom row). For the pristine sample, the Li 1s region exhibits one peak around 54.4 eV, which is attributed to Li in the NCM structure.^[82] The F 1s region shows no signal as no fluorine species have been used for the preparation of the thin films. When exposed to LP30 for 72 h and subsequently washed with conductive salt free EC:DMC, two weak Li 1s signals are detected around 54.4 eV and 56.4 eV. The former is again attributed to Li in NCM. The latter lies between the binding energy of Li in LiPF_6 (57.9 eV) and in LiF (around 55.7 eV),^[78] whose position was determined by XPS measurements of LiPF_6 powder (Figure S5, Supporting Information). The signal at 56.4 eV is attributed to a lithium oxyfluorophosphate species $\text{Li}_x\text{PO}_y\text{F}_z$ forming on the surface of the oxide coating when being exposed to the LiPF_6 containing electrolyte. The signals present in the F 1s region support this assignment. Two species can be distinguished: one at 685.1 eV and one at 687.7 eV, whereas the latter corresponds to $\text{Li}_x\text{PO}_y\text{F}_z$.^[79,81] The assignment of the signal at around 685.1 eV is more complicated, since several metal fluorides exhibit a F 1s signal at these binding energies, including Li, Ni, Mn, and Co.^[83,84] Only LiF can be excluded as we observe no corresponding peak in the Li 1s region. After charging and discharging for 20 cycles, the Li 1s exhibits again two small peaks. Deconvolution reveals two species located around 54.4 eV and 55.8 eV. While the more intense species at around 54.4 eV corresponds to Li in NCM, the signal around 55.8 eV is attributed to LiF, which forms during cycling and is part of the CEI.^[9,85]

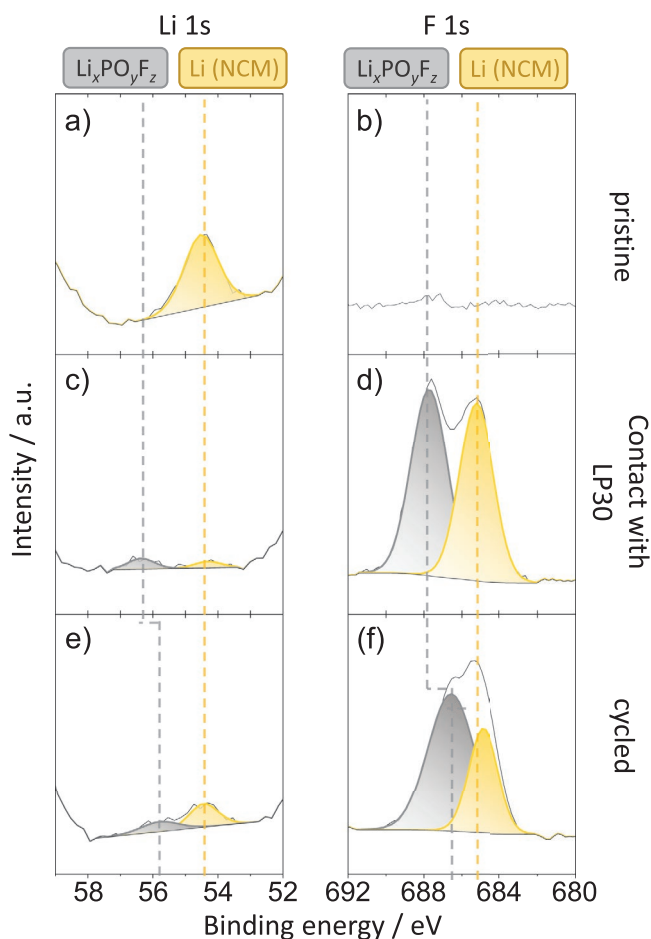


Figure 6. XPS analysis of an uncoated thin film cathode in the Li 1s (left column) and the F 1s (right column) region. The top row shows the pristine state, the middle row shows the state after contact with the electrolyte LP30, and the bottom row shows the cycled state of the thin film cathode.

The formation of LiF also contributes to the signal at around 684.9 eV in the F 1s region. Again, we attribute the second F 1s signal to a $\text{Li}_x\text{PO}_y\text{F}_z$ species. Compared to the sample in contact with the electrolyte, the $\text{Li}_x\text{PO}_y\text{F}_z$ signal is shifted to a higher binding energy of about 686.6 eV indicating a lower amount of fluorine or a higher amount of oxygen. The results confirm small amounts of Li containing oxyfluorophosphates are formed on the surface of NCM in contact with LP30 electrolyte, while LiF is only formed during cycling. Both reactions result in the degradation of the active material and the formation of a resistive CEI, which is responsible for the observed capacity fading.

Figure 7 shows the results of the XPS analysis of the Al_2O_3 -coated thin film. Similar to the uncoated NCM thin film, the Li 1s region (Figure 7a) for the pristine Al_2O_3 -coated thin film exhibits only one peak around 54.2 eV, which corresponds to Li in the transition metal oxide as discussed above. There is also a small bump in the F 1s region of the pristine sample (Figure 7b), which we attribute to fluorine contamination inside the measurement setup as no fluorine species are involved in the synthesis of the thin films. The Al 2p region for the pristine

alumina coated NCM thin film (Figure 7c) experiences a single peak around 74.1 eV that corresponds to Al_2O_3 . After exposure to LP30, a second peak around 56.3 eV appears in the Li 1s signal (Figure 7d), which is again attributed to a $\text{Li}_x\text{PO}_y\text{F}_z$ species forming on the coating according to Equation (3). The binding energy is in agreement with the species measured for the pristine uncoated sample (Figure 7a). The corresponding F 1s signal (Figure 7e) exhibits a peak at around 686.2 eV, which is attributed to AlF_3 . Additionally, a small shoulder at higher binding energies is visible. Deconvolution yields a binding energy of about 688.1 eV revealing the formation of a lithium oxyfluorophosphate species on the oxide coating. It is worth noting that the binding energy of the lithium oxyfluorophosphate species slightly differs from the one formed in case of the uncoated sample due to a different nature of coordination. This indicates that the electrons of the 1s state of F and Li experience a stronger Coulomb interaction. After treatment with LP30, the Al 2p signal (Figure 7f) displays a single peak that is shifted toward a higher binding energy compared to the pristine sample. Deconvolution reveals the presence of a second species around 74.9 eV in addition to the Al_2O_3 species at 74.1 eV. Kim et al. analyzed fluorinated alumina surfaces with varying fluorine content.^[86] According to their results, the species around 74.9 eV is an aluminum oxyfluoride, that is, a not fully fluorinated oxide, whose formation is expected from Equation (1). No additional species are detectable after electrochemical cycling and the intensity ratio of the different species detected in the Li 1s (Figure 7g) and F 1s region (Figure 7h) exhibit minor to no changes. The ratio of Al_2O_3 and AlO_xF_y also experiences only minor changes during cycling after the initial fluorination (Figure 8). The results show the formation of a passivating aluminum oxyfluoride layer on the Al_2O_3 coating when getting into contact with the electrolyte in agreement with the thermodynamic calculations. In addition, no changes in composition of the surface species occur during cycling revealing the formation of a highly stable CEI. The results confirm that the passivated coating protects the surface from HF corrosion and stabilizes the electrochemical performance of the thin film cathode in the long run.

Figure 9 shows the results of the XPS analysis of the pristine CeO_2 -coated cathode thin film, after exposure to the liquid electrolyte for 72 h, and after electrochemical cycling. The Li 1s region of the pristine cathode (Figure 9a) exhibits only the Li peak at 54.4 eV from the NCM structure as for the uncoated and the Al_2O_3 -coated thin film. The F 1s region (Figure 9b) only exhibits a minor peak, which is visible in due to fluorine contamination inside the vacuum chamber. The analysis of the Ce 3d region (Figure 9c) is more difficult due to multiplet splitting and the presence of the oxidation states Ce^{3+} and Ce^{4+} . In total, six signals originating from CeO_2 (v, v', v'' and u, u', u'' at 882.2, 888.6, 898.1 eV and 900.7, 907.0, 916.6 eV, respectively) and four additional signals from Ce_2O_3 (v_0, v' and u_0, u' at 881.1, 884.8 eV and 899.4, 902.9 eV, respectively) must be taken into account. For a reliable analysis of the XPS spectra of the CeO_2 coating, it is important to consider that ceria is partly reduced to $\text{CeO}_{2-\delta}$ when introduced to the high vacuum chamber of the XPS system. Therefore, we analyzed the Ce 3d region of the XPS spectra after 0, 20, and 40 min after introducing the sample into the chamber (Figure S6, Supporting Information).

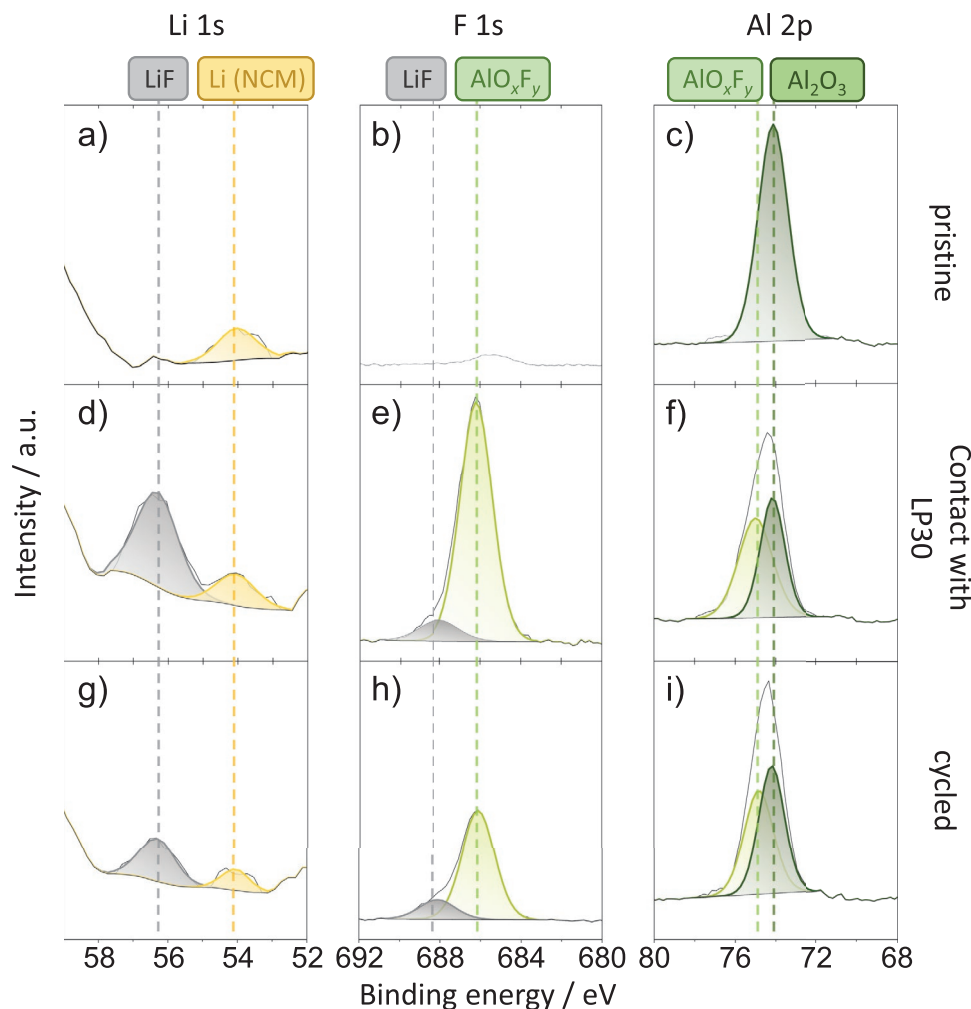


Figure 7. XPS analysis of an Al_2O_3 -coated thin film cathode in the Li 1s (left column) and the F 1s (middle column) and the Al 2p (right column) region. The top row shows the pristine state, the middle row exhibits the state after contact with electrolyte LP30, and the bottom row shows the cycled state of the thin film.

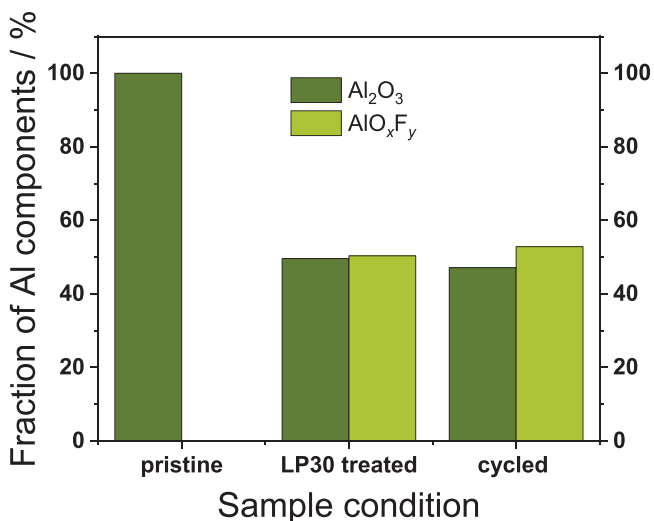


Figure 8. Evaluation of the Al 2p region of Al_2O_3 -coated thin film cathodes under different conditions.

Using principal component analysis (PCA) allows for a reliable deconvolution of the Ce^{3+} and Ce^{4+} signals from the CeO_2 coating grown by ALD on the NCM thin film (Figure 9c). The corresponding signals exhibit a splitting energy of 18.45 eV, which is in accordance with previously reported work on ceria thin films.^[53,55] The XPS analysis reveal that the pristine coating layer consists of about 80% Ce^{4+} and 20% Ce^{3+} (Figure 10).

The Li 1s signal (Figure 9d) exhibits a second signal at around 56.3 eV in addition to the Li signal at 54.4 eV after exposure to the electrolyte for 72 h. This second peak indicates the presence of a lithium oxyfluorophosphate comparable to the species detected for the Al_2O_3 -coated thin film cathode (Figure 9d). The formation of a lithium oxyfluorophosphate species is supported by the presence of the peak at 687.0 eV in the F 1s region (Figure 9e). A second peak in the F 1s region arises at 684.4 eV, which we attribute to cerium fluoride based on the XPS analysis of a CeF_4 reference powder (Figure S7, Supporting Information). Thus, the XPS results support the formation of CeF_4 and PO_2F_2 as proposed by Equation (4). However, the assignment of the F 1s signal at 684.4 eV is not

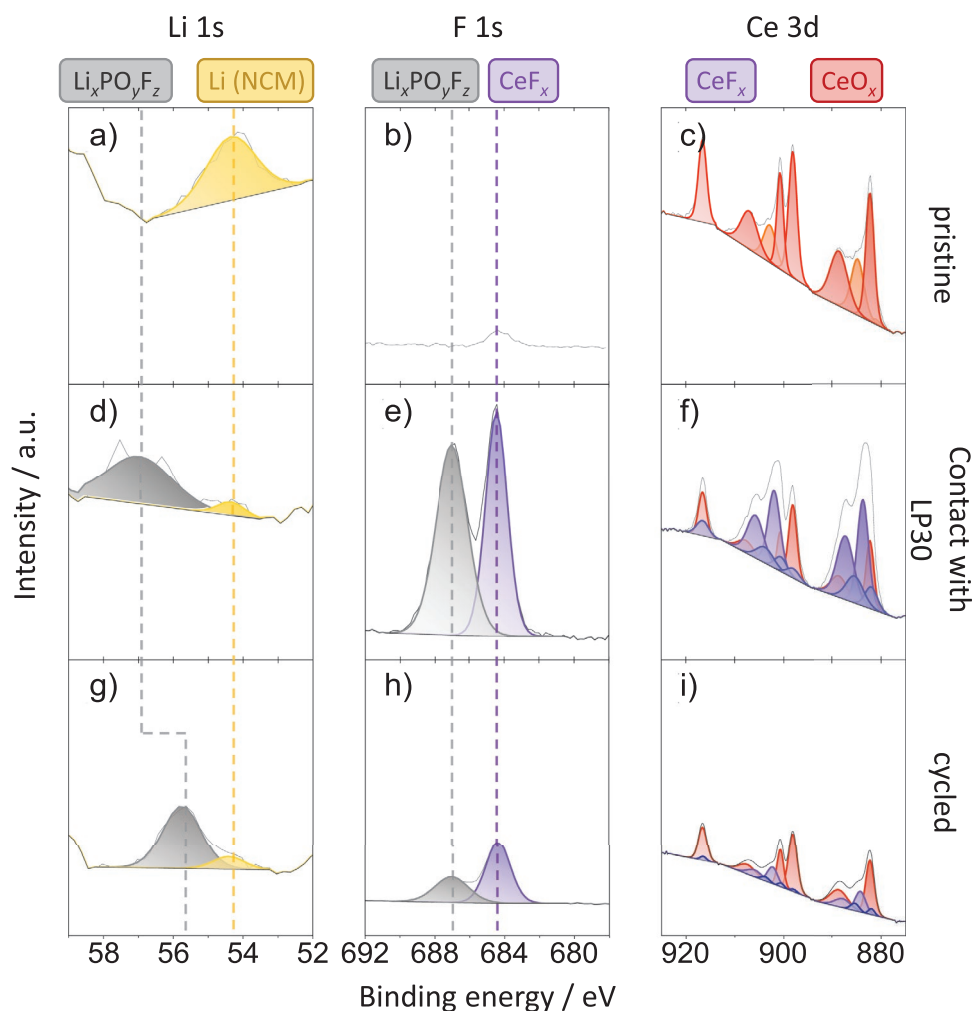


Figure 9. Results of the XPS analysis of a CeO_2 -coated thin film cathode. Depicted are the Li 1s (left column) and the F 1s (middle column) and the Ce 3d (right column) region, with the pristine state in the top row, the middle row exhibiting the state after contact with electrolyte LP30, and the bottom row showing the cycled state of the thin film.

straightforward, as transition metal and lithium fluorides also exhibit signals in this energy range (around 684.6 eV), which makes the deconvolution challenging. Analysis of the Ce 3d region is therefore necessary to confirm the formation of cerium fluoride at the coating surface. CeF_4 exhibits different oxidation states and multiplet splitting yielding up to ten peaks in the Ce 3d region. Taking into account that the CeO_2 coating only gets partly fluorinated, the presence of the additional ten peaks arising from CeO_2 needs to be considered, too. PCA of the Ce 3d region of a CeF_4 powder sample provides reliable reference data for the Ce^{3+} and Ce^{4+} signals (Figure S7, Supporting Information). Similar to CeO_2 , CeF_4 decomposes into CeF_3 when exposed to vacuum and X-ray radiation. The fitting process resulted in four components for CeF_3 at 883.7, 887.2, 902.0, and 905.8 eV, and six components for CeF_4 at 882.0, 885.4, 898.0, 900.6, 903.8, and 916.6 eV. Based on these results, the Ce 3d region of the CeO_2 -coated thin film cathode exposed to LP30 for 72 h (Figure 9f) reveals the presence of CeO_2 (30% of the total amount Ce), CeF_3 (51%), and CeF_4 (19%). The residual signatures associated with CeO_2 imply that the coating is not

completely fluorinated. Interestingly, the amount of Ce^{3+} fluoride exceeds the amount of Ce^{4+} fluoride (Figure 10) although CeF_4 is the thermodynamically more stable component. This might be due to the vacuum conditions in the XPS chamber as we observed this for the reference sample as well. However, the measurements confirm the formation of cerium fluoride after contact with LP30. After electrochemical cycling for 20 cycles, the Li 1s still exhibits the species corresponding to Li in NCM at 55.4 eV (Figure 9g). The second, larger peak at 55.7 eV arises from LiF. In the F 1s region (Figure 9h), both peaks measured after exposure to LP30 for 72 h are still present after cycling. Since the shift in the Li 1s signal is apparent and indicates the formation of LiF, we attribute the signal at 684.4 eV partly to LiF. The peak at around 687.0 eV is in the same binding energy range as the one attributed to lithium oxyfluorophosphate. A Li free oxyfluorophosphate seems to be formed during cycling as no corresponding peak is detectable in the Li 1s region. The Ce 3d region (Figure 9i) exhibits the same signals as after exposure to LP30. However, the intensities of the Ce^{3+} and Ce^{4+} fluoride signals decrease compared to the intensities of the

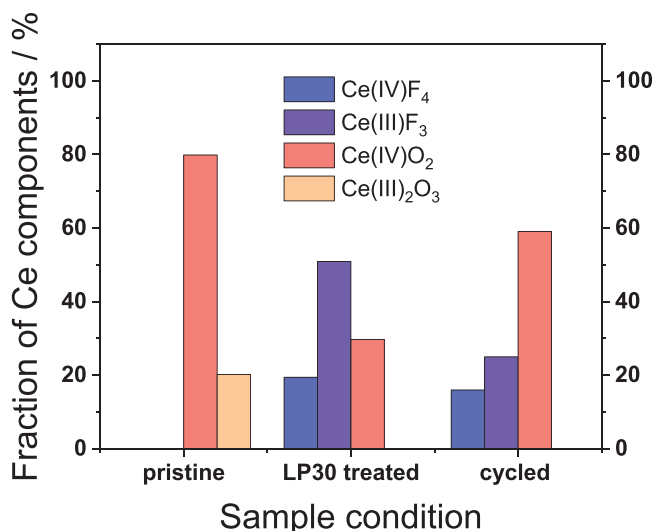


Figure 10. Evaluation of the Ce 3d region of CeO₂-coated thin film cathodes under different conditions as a fraction of Ce components.

corresponding CeO_{2,δ} signals. This indicates a lower amount of the CeF₄ compounds (Figure 10). It is evident from the ratio of the total amount of the Ce compounds that the fraction of CeF₃ decreases, while the fraction of CeO₂ increases. The fraction of CeF₄ remains constant. This shows that CeF₃ converts back to CeO₂ during cycling, possibly due to the release of oxygen from the cathode material, which is known to happen during cycling.^[87,88] However, it is also possible to interpret changes in the integrated peak intensity (Figure S8, Supporting Information), which is used to calculate the ratio. The integrated peak intensity of the CeO₂ signals stays rather constant, while those of the CeF₃ and CeF₄ signals decrease by 78% and 63%, respectively. Thus, cerium fluoride seems to detach from the surface during cycling. However, the XPS results reveal that the CEI components undergo changes during cycling, that is, the CEI is less stable as for the Al₂O₃-coated thin film, which is expected from the lower Gibbs free energy $\Delta G_{\text{CeO}_2}^\circ = -26 \text{ kJ mol}^{-1}$. This instability explains the decrease in capacity over time. As the coating is dissolved, areas of the cathode material get exposed to harmful species in the electrolyte and the cathode material degrades.

3. Conclusions

In this paper, we investigated the surface stability and the reaction products of Al₂O₃ and CeO₂-coated NCM111 thin film cathodes during cycling. Electrochemical characterization confirms the beneficial effect of the Al₂O₃ coating on the long term cycling performance of the cathodes, whereas the CeO₂-coated thin film shows an even worse cell performance than the uncoated cathode. Impedance measurements reveal an increased charge transfer resistance for both coated cathodes as the coating and the formation of a CEI deteriorates lithium ion exchange with the electrolyte. The differences in cycling performance of the three cathodes are correlated with the structural stability of the coating layer. XPS analysis confirms the

formation of a CEI in case of the uncoated cathode, which is composed of the reaction products from electrolyte decomposition and dissolved transition metal ions. The degradation of the cathode active material is responsible for the observed capacity fading. In addition, the XPS analysis reveals that a spontaneous fluorination reaction between coating and the conductive salt LiPF₆ occurs for both coatings. For the Al₂O₃-coated thin film, the fluorination acts as a passivation, hindering HF attack and effectively protecting the cathode active material from degradation. In contrast, the fluorinated CeO₂ coating is less stable against corrosion leading to surface degradation during cycling and a worse electrochemical performance of the corresponding cell. The results emphasize that a high chemical stability is mandatory for appropriate coatings in order to prevent surface degradation of the cathode active material.

4. Experimental Section

Thin Film Preparation and Coating: The model thin film cathodes were prepared via a sol-gel approach using spin-coating as described in ref. [30]. In brief, stoichiometric amounts of lithium nitrate (LiNO₃·H₂O, 99.99%), nickel (II) nitrate hexahydrate (Ni(NO₃)₂·6 H₂O, 99.999%), cobalt (II) nitrate hexahydrate (Co(NO₃)₂·6 H₂O, 99.999%), manganese (II) nitrate tetrahydrate (Mn(NO₃)₂·4 H₂O, 99.99%), and 150 mg polyvinylpyrrolidone (PVP, average molecular weight of 40 000) were dissolved in a mixture of 0.5 mL deionized water and 3.5 mL ethanol. Subsequently, the mixture was deposited on a Pt-coated (100 nm) sapphire substrate using spin-coating (3000 rpm, 45 s). All chemicals were purchased from Sigma Aldrich. The as-prepared NCM thin films were coated with an ultrathin and homogenous surface layer using ALD. ALD enables growth with atomic-level thickness control and high conformity yielding dense coatings even on porous substrates.^[53,55,89] The Al₂O₃ and CeO₂ coatings were deposited in a commercial thermal ALD system (Picosun R200 Standard) at 250 °C. Trimethylaluminum (TMA, STREM Chemicals., min. 98%) and deionized water (DI-H₂O) were used as precursors for the deposition of the aluminum oxide. TMA and DI-H₂O were pulsed for 0.5 and 3 s, respectively, and the system was purged with Argon for 10 s after each precursor pulse. 20 cycles resulted in an Al₂O₃ layer of ≈2 nm thickness.^[30,32] Tetrakis(2,2,6,6-tetramethyl-3,5-heptanedionato)cerium(IV) (Ce(TMHD)₄, STREM Chemicals, min. 97%) and ozone, which was produced by an ozone generator (AC-2025, Teledyne API), were used as precursors for the CeO₂ deposition. The precursor Ce(TMHD)₄ was kept at 235 °C. Each, Ce(TMHD)₄ and ozone were pulsed for 2 s, and each pulse was followed by a 60 s Ar purge step. 63 cycles resulted in a CeO₂ layer of ≈2 nm thickness.^[53–55] A Si wafer was additionally placed in the ALD reaction chamber, which allowed the determination of the thickness of the deposited thin films using X-ray reflectivity (Siemens/Bruker D5000 X-ray diffraction system).

Electrochemical Characterization: Assembly of the pouch bag cells was carried out in an Ar filled glove box to ensure oxygen and water levels below 1 ppm. A half-cell setup, using metallic lithium (100 μm thickness, Albetmarle Germany GmbH) as counter and reference electrode, was chosen for the electrochemical characterization of the uncoated and coated NCM thin film model systems. The cathode thin films acted as the working electrode. Separation of the electrodes was achieved by using two Whatman glass fiber separator (GF-A) soaked with 120 μL of electrolyte (1 M LiPF₆ as conducting salt in EC/DMC, LP30, battery grade, ≤ 15 ppm, Sigma Aldrich). Electrochemical analysis was performed using a VMP300 potentiostat by Biologic. Before measurement, open-circuit voltage (OCV) measurements were carried out to ensure equilibrium inside the cell. To guarantee comparability between the different cathode thin films and the cell performance, the measurement was conducted as follows: after measuring OCV for 30 min, the cells were charged to 4.2 V versus Li/Li⁺ with a constant current of 1.5 μA. After charging, the cells were discharged with 1.5 μA

to 4.0 V versus Li/Li⁺ and kept at the potential for 2 h to ensure that equilibrium was reached. Potentiostatic electrochemical impedance spectroscopy (PEIS) between 10 mHz and 100 kHz with an amplitude of 10 mV was performed at 4.0 V versus Li/Li⁺. Subsequently, the cells were discharged further with 1.5 μA to a potential of 3.0 V versus Li/Li⁺. All measurements were performed at room temperature. For the post-mortem characterization the electrochemical cells were disassembled, the cathode films were rinsed five times with DMC, and subsequently dried at 60 °C for 18 h.

Structural Characterization: For the morphological analysis of the surface a Zeiss SMT Merlin high resolution Schottky field-emission scanning electron microscope (HRSEM) was used with a voltage of 3 kV and an emission current of 100 pA. Images were taken in high resolution mode with a magnification of 10,000 and a working distance of 5 mm. X-ray photoelectron spectroscopy (XPS) was performed using a PHI5000 Versa Probe II. Using a transfer vessel the samples were kept under Ar during the introduction into the XPS system. A monochromatic Al K α source ($h\nu = 1486.6$ eV, 100 W) with a spot size of 5×5 μm was used for analysis, utilizing a dual beam charge neutralizer to avoid charging effects. The pass energy used for the detail spectra was 23.5 eV with a step size of 0.2 eV. All spectra were calibrated to the signal of adventitious carbon (284.8 eV). Analysis of the acquired data was done using CasaXPS version 2.3.25.^[90]

Supporting Information

Supporting Information is available from the Wiley Online Library or from the author.

Acknowledgements

H.H. and M.T.E. thank the German Federal Ministry of Education and Research (BMBF) for providing the funding support from the NanoMatFutur project NiKo (03XP0093) as well as Neal Fairley for helping in the interpretation of the XPS measurements. M.T.E. acknowledges financial support from the German Research Foundation (DFG) via the Heisenberg Program (Grant EL 863/6-1). P.K. and S.C. acknowledges financial support from the German Research Foundation (DFG) via the collaborative research center SFB 1083 (project-ID 223848855).

Open access funding enabled and organized by Projekt DEAL.

Conflict of Interest

The authors declare no conflict of interest.

Data Availability Statement

The data that support the findings of this study are available from the corresponding author upon reasonable request.

Keywords

atomic layer deposition, lithium-ion battery, nickel cobalt manganese oxides cathode, oxide coatings, surface degradation, thin film cathode, X-ray photoelectron spectroscopy

Received: October 24, 2022

Revised: December 21, 2022

Published online: February 17, 2023

- [1] K. Mizushima, P. C. Jones, P. J. Wiseman, J. B. Goodenough, *Solid State Ionics* **1981**, 3–4, 171.
- [2] Y. Ding, R. Wang, L. Wang, K. Cheng, Z. Zhao, D. Mu, B. Wu, *Energy Procedia* **2017**, 105, 2941.
- [3] A. Manthiram, B. Song, W. Li, *Energy Storage Mater.* **2017**, 6, 125.
- [4] J. Kim, H. Ma, H. Cha, H. Lee, J. Sung, M. Seo, P. Oh, M. Park, J. Cho, *Energy Environ. Sci.* **2018**, 11, 1449.
- [5] Y. Ding, D. Mu, B. Wu, R. Wang, Z. Zhao, F. Wu, *Appl. Energy* **2017**, 195, 586.
- [6] N. Nitta, F. Wu, J. T. Lee, G. Yushin, *Mater. Today* **2015**, 18, 252.
- [7] W. Li, B. Song, A. Manthiram, *Chem. Soc. Rev.* **2017**, 46, 3006.
- [8] S.-K. Jung, H. Gwon, J. Hong, K.-Y. Park, D.-H. Seo, H. Kim, J. Hyun, W. Yang, K. Kang, *Adv. Energy Mater.* **2014**, 4, 1300787.
- [9] K. Edström, T. Gustafsson, J. O. Thomas, *Electrochim. Acta* **2004**, 50, 397.
- [10] C. L. Campion, W. Li, B. L. Lucht, *J. Electrochem. Soc.* **2005**, 152, A2327.
- [11] N. P. W. Pieczonka, Z. Liu, P. Lu, K. L. Olson, J. Moote, B. R. Powell, J.-H. Kim, *J. Phys. Chem. C* **2013**, 117, 15947.
- [12] Y. Qin, D. Wang, M. Liu, C. Shen, Y. Hu, Y. Liu, B. Guo, *ACS Appl. Mater. Interfaces* **2021**, 13, 49445.
- [13] K. Matsumoto, K. Nakahara, K. Inoue, S. Iwasa, K. Nakano, S. Kaneko, H. Ishikawa, K. Utsugi, R. Yuge, *J. Electrochem. Soc.* **2014**, 161, A831.
- [14] M. Lang, M. S. D. Darma, K. Kleiner, L. Riekehr, L. Mereacre, M. Ávila Pérez, V. Liebau, H. Ehrenberg, *J. Power Sources* **2016**, 326, 397.
- [15] M. Evertz, F. Horsthemke, J. Kasnatscheew, M. Börner, M. Winter, S. Nowak, *J. Power Sources* **2016**, 329, 364.
- [16] S. F. F. Lux, I. T. T. Lucas, E. Pollak, S. Passerini, M. Winter, R. Kostecki, *Electrochem. Commun.* **2012**, 14, 47.
- [17] J. Lüchtefeld, H. Hemmelmann, S. Wachs, K. J. Mayrhofer, M. T. Elm, B. B. Berkes, *J. Phys. Chem. C* **2022**, 126, 17204.
- [18] B. S. Parimalam, B. L. Lucht, *J. Electrochem. Soc.* **2018**, 165, A251.
- [19] D. R. Gallus, R. Schmitz, R. Wagner, B. Hoffmann, S. Nowak, I. Cekic-Laskovic, R. W. Schmitz, M. Winter, *Electrochim. Acta* **2014**, 134, 393.
- [20] T. He, Y. Lu, Y. Su, L. Bao, J. Tan, L. Chen, Q. Zhang, W. Li, S. Chen, F. Wu, *ChemSusChem* **2018**, 11, 1639.
- [21] B. Han, B. Key, S. H. Lapidus, J. C. Garcia, H. Iddir, J. T. Vaughey, F. Dogan, *ACS Appl. Mater. Interfaces* **2017**, 9, 41291.
- [22] T. Weigel, F. Schipper, E. M. Erickson, F. A. Susai, B. Markovsky, D. Aurbach, *ACS Energy Lett.* **2019**, 4, 508.
- [23] C. Liang, F. Kong, R. C. Longo, C. Zhang, Y. Nie, Y. Zheng, K. Cho, *J. Mater. Chem. A* **2017**, 5, 25303.
- [24] J. W. Kim, J. J. Travis, E. Hu, K. W. Nam, S. C. Kim, C. S. Kang, J. H. Woo, X. Q. Yang, S. M. George, K. H. Oh, S. J. Cho, S. H. Lee, *J. Power Sources* **2014**, 254, 190.
- [25] C. L. Liao, Y. H. Lee, K. Z. Fung, *J. Alloys Compd.* **2007**, 436, 303.
- [26] K. X. Wang, X. H. Li, J. S. Chen, *Adv. Mater.* **2015**, 27, 527.
- [27] W. Sun, M. Xie, X. Shi, L. Zhang, *Mater. Res. Bull.* **2015**, 61, 287.
- [28] K. Liu, G. L. Yang, Y. Dong, T. Shi, L. Chen, *J. Power Sources* **2015**, 281, 370.
- [29] S. Dong, Y. Zhou, C. Hai, J. Zeng, Y. Sun, Y. Shen, X. Li, X. Ren, G. Qi, X. Zhang, L. Ma, *Ceram. Int.* **2019**, 45, 144.
- [30] H. Hemmelmann, J. K. Dinter, M. T. Elm, *Adv. Mater. Interfaces* **2021**, 8, 2002074.
- [31] R. S. Negi, S. P. Culver, A. Mazilkin, T. Brezesinski, M. T. Elm, *ACS Appl. Mater. Interfaces* **2020**, 12, 31392.
- [32] R. S. Negi, S. P. Culver, M. Wiche, S. Ahmed, K. Volz, M. T. Elm, *Phys. Chem. Chem. Phys.* **2021**, 23, 6725.
- [33] R. S. Negi, E. Celik, R. Pan, R. Stäglich, J. Senker, M. T. Elm, *ACS Appl. Energy Mater.* **2021**, 4, 3369.
- [34] N. D. Phillip, R. E. Ruther, X. Sang, Y. Wang, R. R. Unocic, A. S. Westover, C. Daniel, G. M. Veith, *ACS Appl. Energy Mater.* **2019**, 2, 1405.

- [35] K. T. Jung, G. B. Cho, K. W. Kim, T. H. Nam, H. M. Jeong, S. C. Huh, H. S. Chung, J. P. Noh, *Thin Solid Films* **2013**, 546, 414.
- [36] Y. J. Kim, H. Kim, B. Kim, D. Ahn, J. G. Lee, T. J. Kim, D. Son, J. Cho, Y. W. Kim, B. Park, *Chem. Mater.* **2003**, 15, 1505.
- [37] L. Nation, J. Li, C. James, Y. Qi, N. Dudley, B. W. Sheldon, *J. Power Sources* **2017**, 364, 383.
- [38] R. Azmi, V. Trouillet, M. Strafela, S. Ulrich, H. Ehrenberg, M. Bruns, *Surf. Interface Anal.* **2018**, 50, 43.
- [39] W. Liu, X. Li, D. Xiong, Y. Hao, J. Li, H. Kou, B. Yan, D. Li, S. Lu, A. Koo, K. Adair, X. Sun, *Nano Energy* **2018**, 44, 111.
- [40] Y. S. Jung, A. S. Cavanagh, A. C. Dillon, M. D. Groner, S. M. George, S.-H. Lee, *J. Electrochem. Soc.* **2010**, 157, A75.
- [41] Y. S. Jung, A. S. Cavanagh, L. A. Riley, S. H. Kang, A. C. Dillon, M. D. Groner, S. M. George, S. H. Lee, *Adv. Mater.* **2010**, 22, 2172.
- [42] D. Guan, J. A. Jeevarajan, Y. Wang, *Nanoscale* **2011**, 3, 1465.
- [43] R. L. Patel, H. Xie, J. Park, H. Y. Asl, A. Choudhury, X. Liang, *Adv. Mater. Interfaces* **2015**, 2, 1570039.
- [44] D. S. Hall, R. Gauthier, A. Eldesoky, V. S. Murray, J. R. Dahn, *ACS Appl. Mater. Interfaces* **2019**, 11, 14095.
- [45] C. C. Wang, A. Manthiram, *J. Mater. Chem. A* **2013**, 1, 10209.
- [46] M. R. Laskar, D. H. K. Jackson, S. Xu, R. J. Hamers, D. Morgan, T. F. Kuech, *ACS Appl. Mater. Interfaces* **2017**, 9, 11231.
- [47] J. Kasnatscheew, U. Rodehorst, B. Streipert, S. Wiemers-Meyer, R. Jakelski, R. Wagner, I. C. Laskovic, M. Winter, *J. Electrochem. Soc.* **2016**, 163, A2943.
- [48] J. Kasnatscheew, M. Evertz, B. Streipert, R. Wagner, R. Klöpsch, B. Vortmann, H. Hahn, S. Nowak, M. Amereller, A. C. Gentschev, P. Lamp, M. Winter, *Phys. Chem. Chem. Phys.* **2016**, 18, 3956.
- [49] Y. Oh, D. Ahn, S. Nam, B. Park, *J. Solid State Electrochem.* **2010**, 14, 1235.
- [50] Y. Su, S. Cui, Z. Zhuo, W. Yang, X. Wang, F. Pan, *ACS Appl. Mater. Interfaces* **2015**, 7, 25105.
- [51] N. Dannehl, S. O. Steinmüller, D. V. Szabó, M. Pein, F. Sigel, L. Esmezjan, U. Hasenkox, B. Schwarz, S. Indris, H. Ehrenberg, *ACS Appl. Mater. Interfaces* **2018**, 10, 43131.
- [52] R. S. Negi, Y. Yusim, R. Pan, S. Ahmed, K. Volz, R. Takata, F. Schmidt, A. Henss, M. T. Elm, *Adv. Mater. Interfaces* **2022**, 9, 2101428.
- [53] M. F. Zscherp, J. Glaser, C. Becker, A. Beyer, P. Cop, J. Schörmann, K. Volz, M. T. Elm, *Cryst. Growth Des.* **2020**, 20, 2194.
- [54] E. Celik, P. Cop, R. S. Negi, A. Mazilkin, Y. Ma, P. Klement, J. Schörmann, S. Chatterjee, T. Brezesinski, M. T. Elm, *ACS Nano* **2022**, 16, 3182.
- [55] P. Cop, E. Celik, K. Hess, Y. Moryson, P. Klement, M. T. Elm, B. M. Smarsly, *ACS Appl. Nano Mater.* **2020**, 3, 10757.
- [56] C. Ho, I. D. Raistrick, R. A. Huggins, *J. Electrochem. Soc.* **1980**, 127, 343.
- [57] R. Ruess, S. Schweidler, H. Hemmelmann, G. Conforto, A. Bielefeld, D. A. Weber, J. Sann, M. T. Elm, J. Janek, *J. Electrochem. Soc.* **2020**, 167, 100532.
- [58] S. Skale, V. Doleček, M. Slemnik, *Corros. Sci.* **2007**, 49, 1045.
- [59] J. Huang, *Electrochim. Acta* **2018**, 281, 170.
- [60] M. D. Levi, D. Aurbach, *J. Phys. Chem. B* **2004**, 108, 11693.
- [61] H. Nara, K. Morita, D. Mukoyama, T. Yokoshima, T. Momma, T. Osaka, *Electrochim. Acta* **2017**, 241, 323.
- [62] S. Rodrigues, N. Munichandraiah, A. K. Shukla, *J. Power Sources* **2000**, 87, 12.
- [63] S.-B. Son, D. Robertson, Y. Tsai, S. Trask, A. Dunlop, I. Bloom, *J. Electrochem. Soc.* **2020**, 167, 160508.
- [64] R. Sahore, F. Dogan, I. D. Bloom, *Chem. Mater.* **2019**, 31, 2884.
- [65] W. Cao, Q. Li, X. Yu, H. Li, *eScience* **2022**, 2, 47.
- [66] J. Fleig, *Solid State Ionics* **2002**, 150, 181.
- [67] X. Guo, Z. Zhang, *Acta Mater.* **2003**, 51, 2539.
- [68] M. T. Elm, J. D. Hofmann, C. Suchomski, J. Janek, T. Brezesinski, *ACS Appl. Mater. Interfaces* **2015**, 7, 11792.
- [69] H.-R. Kim, S.-G. Woo, J.-H. Kim, W. Cho, Y.-J. Kim, *J. Electroanal. Chem.* **2016**, 782, 168.
- [70] K. Ishidzu, Y. Oka, T. Nakamura, *Solid State Ionics* **2016**, 288, 176.
- [71] H.-H. Ryu, K.-J. Park, C. S. Yoon, Y.-K. Sun, *Chem. Mater.* **2018**, 30, 1155.
- [72] S. T. Myung, K. Izumi, S. Komaba, Y. K. Sun, H. Yashiro, N. Kumagai, *Chem. Mater.* **2005**, 17, 3695.
- [73] G. Vinothkumar, S. Rengaraj, P. Arunkumar, S. W. Cha, K. Suresh Babu, *J. Phys. Chem. C* **2019**, 123, 541.
- [74] K. Michel, J.-P. Eufinger, G. Ulbrich, M. Lerch, J. Janek, M. T. Elm, *Phys. Chem. Chem. Phys.* **2017**, 19, 17661.
- [75] S. Omar, J. C. Nino, *Acta Mater.* **2013**, 61, 5406.
- [76] D. Marrocchelli, S. R. Bishop, H. L. Tuller, B. Yildiz, *Adv. Funct. Mater.* **2012**, 22, 1958.
- [77] H. L. Tuller, S. R. Bishop, *Annu. Rev. Mater. Res.* **2011**, 41, 369.
- [78] M. L. Williams, *Occup. Environ. Med.* **1996**, 53, 504.
- [79] L. Ma, L. Ellis, S. L. Glazier, X. Ma, Q. Liu, J. Li, J. R. Dahn, *J. Electrochem. Soc.* **2018**, 165, A891.
- [80] W. Zhao, G. Zheng, M. Lin, W. Zhao, D. Li, X. Guan, Y. Ji, G. F. Ortiz, Y. Yang, *J. Power Sources* **2018**, 380, 149.
- [81] G. Yang, J. Shi, C. Shen, S. Wang, L. Xia, H. Hu, H. Luo, Y. Xia, Z. Liu, *RSC Adv.* **2017**, 7, 26052.
- [82] J. C. Dupin, D. Gonbeau, H. Benqlilou-Moudden, P. Vinatier, A. Levasseur, *Thin Solid Films* **2001**, 384, 23.
- [83] J. F. Moulder, W. F. Stickle, P. E. Sobol, K. D. Bomben, *The Handbook of X-ray Photoelectron-Spectroscopy* (Ed: J. Chastain), Perkin-Elmer Corporation, Eden Prairie **1995**.
- [84] M. Pietrowski, M. Zieliński, E. Alwin, A. Suchora, J. Gawarecka, *RSC Adv.* **2019**, 9, 5711.
- [85] M. Gauthier, T. J. Carney, A. Grimaud, L. Giordano, N. Pour, H.-H. Chang, D. P. Fenning, S. F. Lux, O. Paschos, C. Bauer, F. Maglia, S. Lupart, P. Lamp, Y. Shao-Horn, *J. Phys. Chem. Lett.* **2015**, 6, 4653.
- [86] D. S. Kim, Y. Y. Yu, K. Char, *J. Appl. Phys.* **2004**, 96, 2278.
- [87] R. Jung, M. Metzger, F. Maglia, C. Stinner, H. A. Gasteiger, *J. Electrochem. Soc.* **2017**, 164, A1361.
- [88] J. Wandt, A. T. S. Freiberg, A. Ogrodnik, H. A. Gasteiger, *Mater. Today* **2018**, 21, 825.
- [89] E. Celik, R. S. Negi, M. Bastianello, D. Boll, A. Mazilkin, T. Brezesinski, M. T. Elm, *Phys. Chem. Chem. Phys.* **2020**, 22, 11519.
- [90] N. Fairley, V. Fernandez, M. Richard-Plouet, C. Guillot-Deudon, J. Walton, E. Smith, D. Flahaut, M. Greiner, M. Biesinger, S. Tougaard, D. Morgan, J. Baltrusaitis, *Appl. Surf. Sci. Adv.* **2021**, 5, 100112.